

# Predicting the lattice thermal conductivity of solids by solving the Boltzmann transport equation: AFLOW - AAPL an automated, accurate and efficient framework

Jose J. Plata,<sup>1</sup> Demet Usanmaz,<sup>1</sup> Pinku Nath,<sup>1</sup> Cormac Toher,<sup>1</sup> Jesus Carrete,<sup>2</sup> Mark Asta,<sup>3</sup> Maarten de Jong,<sup>3</sup> Marco Buongiorno Nardelli,<sup>4</sup> Marco Fornari,<sup>5</sup> and Stefano Curtarolo<sup>6</sup>

<sup>1</sup>*Department of Mechanical Engineering and Materials Science,  
Duke University, Durham, North Carolina 27708, USA*

<sup>2</sup>*CEA-Grenoble, 17 Rue des Martyrs, Grenoble 38000, France*

<sup>3</sup>*Department of Materials Science and Engineering, University of California,  
Berkeley, 210 Hearst Memorial Mining Building, Berkeley, USA*

<sup>4</sup>*Department of Physics and Department of Chemistry, University of North Texas, Denton TX, USA.*

<sup>5</sup>*Department of Physics, Central Michigan University, Mount Pleasant, MI 48858, USA.*

<sup>6</sup>*Materials Science, Electrical Engineering, Physics and Chemistry, Duke University, Durham NC, 27708\**

(Dated: November 18, 2016)

One of the most accurate approaches for calculating lattice thermal conductivity,  $\kappa_l$ , is solving the Boltzmann transport equation starting from third-order anharmonic force constants. In addition to the underlying approximations of *ab-initio* parameterization, two main challenges are associated with this path. High computational costs and lack of automation in the frameworks using this methodology affect the discovery rate of novel materials with *ad-hoc* properties. Here, we present the Automatic-Anharmonic-Phonon-Library, AAPL. It efficiently computes interatomic force constants by making effective use of crystal symmetry analysis, it solves the Boltzmann transport equation to obtain  $\kappa_l$ , and allows a fully integrated operation with minimum user intervention, a rational addition to the current high-throughput accelerated materials development framework AFLOW. We show an “experiment *versus* theory” study of the approach, we compare accuracy and speed with respect to other available packages, and for materials characterized by strong electron localization and correlation, we demonstrate that it is possible to improve accuracy without increasing computational requirements by combining AAPL with the pseudo-hybrid functional ACBN0.

PACS numbers: 63.20-e, 63.20.kg, 66.70-f

## I. INTRODUCTION

Lattice thermal conductivity,  $\kappa_l$ , is the key materials’ property for many technologies and applications such as thermoelectricity [1, 2], heat sink materials [3], rewritable density scanning-probe phase-change memories [4] and thermal medical devices [5]. Fast and robust predictions of this quantity remain a challenge [6]: semi-empirical models [7–9] are computationally inexpensive but require some experimental data. Similarly, classical molecular dynamics combined with Green-Kubo relations [10–12] is reasonably quick but requires the knowledge of specific force fields. On the contrary, frameworks based on the quasiharmonic Debye model, such as GIBBS [13] or the AFLOW-Gibbs-Library, AGL [14, 15], are extremely efficient as pre-screening techniques but they lack quantitative accuracy.

The quasiharmonic approximation, QHA, alone has also been used in different models to predict  $\kappa_l$  [6, 16]. Although QHA based models overall improve accuracy of  $\kappa_l$ , they are far from the results obtained from calculating the anharmonic force constants and solving the associated Boltzmann transport equation, BTE [7, 17]. To the best of our knowledge, solving the BTE is the best

method for systematically and accurately calculating thermal conductivity [18–20]. This approach has been successfully applied to many systems during the last decade. It has been recently implemented in packages including Phono3py [21], PhonTS [22], ALAMODE [23], and ShengBTE [24], which compute  $\kappa_l$  by calculating the anharmonic force constants and solving the BTE. Nevertheless, there is a lack of a robust framework, able to calculate  $\kappa_l$  with minimum intervention from the user and therefore targeted to high-throughput automatic and accelerated materials discovery.

Many challenges need to be tackled. **I.** The third order interatomic force constants (IFCs) up to a certain distance cut-off are computationally expensive to obtain from first principles. Overall they represent the major concern for the method. Effective use of crystalline symmetry of the system must be employed to map, through appropriate tensorial transformations, dependent IFCs and therefore reduce the number of calculations. The task is performed by the internal AFLOW point-factor-space group calculator [25]. Recently, it has also been proposed to obtain the IFCs by inverting the results of many entangled calculations with the use of compressive sensing [26]. Further studies need to be carried out to address the scaling of the algorithm with respect to cut-offs and accuracy. **II.** For a rational software for accelerated materials development, all the geometric optimizations, symmetry analyses, su-

\* stefano@duke.edu

percell creation, pre and post-processing, and automatic error corrections to get the IFCs in addition to the appropriate integration for the BTE must be performed by a single code. Here, we present AAPL, which computes the IFCs and solves the BTE to predict  $\kappa_l$  as part of the AFLOW high-throughput framework [27–35], automatizing the entire process. The software is being finalized for an official open-source release during 2017, within the GNU GPL license and, in addition to the AFLOW consortium framework, it will also be implemented inside the Materials Project Ecosystem [36]. **III.** The accuracy of the method mostly depends on the accuracy of the computed forces, and therefore it will inherit the same limitations as the *ab-initio* method used. For materials characterized by strong electron localization and correlation, accurate hybrid functionals for Density Functional Theory parameterizations might not even be feasible as they would drastically increase computational costs, with respect to more basic LDA or GGA functionals. In that case, new strategies should be developed to contain computational demands. Here we give an example: we demonstrate that it is possible to improve the accuracy without increasing computational requirements by combining AAPL with the pseudo-hybrid functional ACBN0 [37–43].

## II. METHODOLOGY: THE AUTOMATIC-ANHARMONIC-PHONON-LIBRARY (AAPL)

**The Boltzmann transport equation.** The Boltzmann equation for phonons, originally formulated by Peierls in 1929, is an important approach for studying phonon transport [7]. Its solution has posed a challenge for the last several decades. Callaway [8] and Allen [44] proposed models based on parameters that are fitted to experimental data. In 2003, Deinzer *et al.* used density functional perturbation theory (DFPT) to study the phonon linewidths of Si and Ge [45]. Since then, many authors have used the solution of the BTE to calculate the lattice thermal conductivity of solids [18–20]. The most used approach is the iterative solution of the BTE proposed by Omini *et al.* and successfully applied in the prediction of the  $\kappa_l$  tensor for different materials [46–48]:

$$\kappa_l^{\alpha\beta} = \frac{1}{N\Omega k_B T^2} \sum_{\lambda} f_0(f_0 + 1)(\hbar\omega_{\lambda})^2 v_{\lambda}^{\alpha} F_{\lambda}^{\beta}, \quad (1)$$

where superscripts  $\alpha$  and  $\beta$  are two of the Cartesian direction indices and the subscript  $\lambda$  comprises both phonon branch index  $i$  and a wave vector  $\mathbf{q}$ . The variables  $\omega_{\lambda}$  and  $\mathbf{v}_{\lambda}$  are the angular frequency and group velocity of the phonon mode  $\lambda$  respectively, while  $f_0(\omega_{\lambda})$  is the phonon distribution function according to Bose-Einstein statistics. All these quantities are obtained through the calculation of the IFCs by using a finite-difference supercell approach: forces *versus* small displacement of inequivalent atoms. In this approach, a reference unit cell of volume  $\Omega$  is used to create the supercell up to the cut-off distance.

For the various summations, the Brillouin zone, BZ, is discretized into a  $\Gamma$ -centered orthogonal regular grid of  $N \equiv N_1 \times N_2 \times N_3$   $\mathbf{q}$ -points, where subscripts 1, 2, and 3 indicate the lattice vector indices.

The mean free displacement  $\mathbf{F}_{\lambda}$  follows the definition of the Bose-Einstein phonon distribution,  $f_{\lambda}$ , in the presence of a temperature gradient  $\nabla T$ . For small perturbations,  $\nabla T \sim 0$ ,  $f_{\lambda}$  can be expanded as  $f_{\lambda} \sim f_0(\omega_{\lambda}) + g_{\lambda}$ , where  $g_{\lambda}$  is the first-order non-equilibrium contribution linear in  $\nabla T$ :

$$g_{\lambda} \equiv -\mathbf{F}_{\lambda} \cdot \nabla T \frac{df_0}{dT}.$$

Finally, the BTE can be expressed as a linear system of equations for  $\mathbf{F}_{\lambda}$ , as [19, 46–50]:

$$\begin{aligned} \mathbf{F}_{\lambda} &= \tau_{\lambda}^0 (\mathbf{v}_{\lambda} + \mathbf{\Delta}_{\lambda}) \\ \mathbf{\Delta}_{\lambda} &= \frac{1}{N} \left( \sum_{\lambda'\lambda''}^{+} \Gamma_{\lambda\lambda'\lambda''}^{+} (\xi_{\lambda\lambda''} \mathbf{F}_{\lambda''} - \xi_{\lambda\lambda'} \mathbf{F}_{\lambda'}) + \right. \\ &\quad \left. + \sum_{\lambda'\lambda''}^{-} \frac{1}{2} \Gamma_{\lambda\lambda'\lambda''}^{-} (\xi_{\lambda\lambda''} \mathbf{F}_{\lambda''} + \xi_{\lambda\lambda'} \mathbf{F}_{\lambda'}) + \right. \\ &\quad \left. + \sum_{\lambda'} \Gamma_{\lambda\lambda'} \xi_{\lambda\lambda'} \mathbf{F}_{\lambda'} \right), \end{aligned} \quad (2)$$

with  $\xi_{\lambda\lambda'} = \omega_{\lambda}/\omega_{\lambda'}$ . The frequently used relaxation time approximation, RTA, corresponds to neglecting the  $\mathbf{\Delta}_{\lambda}$  correction. For the fully solution,  $\mathbf{F}_{\lambda}$  can be self-consistently solved starting from the RTA guess, until convergence of  $\kappa_l$ , Eq. (1). The other quantities present in these formulas, the relaxation time  $\tau_{\lambda}^0$ , and the three-phonon scattering rates  $\Gamma_{\lambda\lambda'\lambda''}^{\pm}$ , will be illustrated in the next Section.

**Vibrational Modes and group velocities.** The vibrational modes are obtained by diagonalizing the dynamical matrix  $D(\mathbf{q})$  [7, 51–53]:

$$D(\mathbf{q})\mathbf{e}_{\lambda} = \omega_{\lambda}^2 \mathbf{e}_{\lambda}; \quad (3)$$

$$D_{ij}^{\alpha\beta}(\mathbf{q}) = \sum_l \frac{\Phi_{ij}^{\alpha\beta}(i, j)}{\sqrt{M(i)M(j)}} \exp[-i\mathbf{q} \cdot (\mathbf{R}_l - \mathbf{R}_0)], \quad (4)$$

where  $M(j)$  is the mass of  $j$ -atom,  $\mathbf{e}_{\lambda}$  is the eigenvector for  $\lambda$ ,  $\mathbf{R}_l$  is the position of lattice point  $l$  and  $\Phi_{ij}^{\alpha\beta}$  are the second-order force constants.  $D(\mathbf{q})$  is a Hermitian  $3n_a \times 3n_a$  matrix, where the factor “3” comes from the dimensionality of the problem, and  $n_a$  represents the number of atoms in the unit cell.

The non-analytical contributions to the dynamical matrix are included by using the formulation of Wang *et al.* [54]:

$$\tilde{D}_{ij}^{\alpha\beta}(\mathbf{q}) = \frac{4\pi e^2}{\Omega} \frac{[\mathbf{q} \cdot \mathbf{Z}(i)]_{\alpha} [\mathbf{q} \cdot \mathbf{Z}(j)]_{\beta}}{\mathbf{q} \cdot \boldsymbol{\epsilon}_{\infty} \cdot \mathbf{q}} \exp[-i\mathbf{q} \cdot (\mathbf{R}_l - \mathbf{R}_0)]. \quad (5)$$

This contribution requires the calculation of the Born effective charge tensors,  $\mathbf{Z}$ , and the high frequency static dielectric tensor,  $\epsilon_\infty$ , i.e. the contribution to the dielectric permittivity tensor from the electronic polarization [55]. Materials with high  $\mathbf{Z}$  and low  $\epsilon_\infty$  are the cases in which the non-analytical contributions are crucial for appropriate description of the phonon spectra as they cause the LO-TO splitting of the spectrum (between longitudinal and transverse optical phonon frequencies) [55].

The group velocities,  $\mathbf{v}_\lambda$ , follow the Hellmann-Feynman theorem:

$$\mathbf{v}_\lambda = \frac{1}{2\omega_\lambda} \left\langle \mathbf{e}_\lambda \left| \frac{\partial D(\mathbf{q})}{\partial \mathbf{q}} \right| \mathbf{e}_\lambda \right\rangle. \quad (6)$$

**Scattering time.** The total scattering time is a sum of terms representing different phenomena:

$$\frac{1}{\tau_\lambda^0} = \frac{1}{\tau_\lambda^{\text{anh}}} + \frac{1}{\tau_\lambda^{\text{iso}}} + \frac{1}{\tau_\lambda^{\text{bnd}}}. \quad (7)$$

$\tau_\lambda^{\text{iso}}$  indicates the isotopic or elastic scattering time and it is due to the isotopic disorder [56, 57]:

$$\begin{aligned} \frac{1}{\tau_\lambda^{\text{iso}}} &= \frac{1}{N} \sum_{\lambda'} \Gamma_{\lambda\lambda'} \\ &= \frac{1}{N} \sum_{\lambda'} \frac{\pi\omega_\lambda^2}{2} \sum_i g(i) |\mathbf{e}_\lambda^*(i) \mathbf{e}_{\lambda'}(i)|^2 \delta(\omega_\lambda - \omega_{\lambda'}), \end{aligned} \quad (8)$$

where  $g(i) = \sum_s f_s(i) [1 - M(i)^s / \overline{M}(i)^s]^2$  is the Pearson deviation coefficient of masses  $M(i)^s$  of isotopes  $s$  for the  $i$  atom,  $f_s$  is the relative fraction of isotope  $s$ , and  $\overline{M}(i)^s$  is the average mass of the element [58].

$\tau_\lambda^{\text{bnd}}$  is the time associated with scattering at the grain boundaries [59, 60],

$$\frac{1}{\tau_\lambda^{\text{bnd}}} = \frac{|\mathbf{v}_\lambda|}{L}, \quad (9)$$

where  $L$  is the average grain size. The effect of the boundaries on  $\kappa_l$  has also been calculated by restricting the summation to the modes with a mean free path,  $\Lambda = \mathbf{F}_\lambda \cdot \mathbf{v}_\lambda / |\mathbf{v}_\lambda|$ , shorter than  $L$  [24]:

$$\kappa_{l,(\Lambda < L)}^{\alpha\beta} = \frac{1}{N\Omega k_B T^2} \sum_{\lambda}^{\Lambda_\lambda < L} f_0(f_0 + 1) (\hbar\omega_\lambda)^2 v_\lambda^\alpha F_\lambda^\beta. \quad (10)$$

$\tau_\lambda^{\text{anh}}$  is the three-phonon scattering time. It is the largest contribution to  $\tau_\lambda^0$  for single crystals at medium-temperature ranges and it is the most computationally expensive quantity to obtain:

$$\frac{1}{\tau_\lambda^{\text{anh}}} = \frac{1}{N} \left( \sum_{\lambda'\lambda''}^+ \Gamma_{\lambda\lambda'\lambda''}^+ + \sum_{\lambda'\lambda''}^- \frac{1}{2} \Gamma_{\lambda\lambda'\lambda''}^- \right). \quad (11)$$

Conservation of the quasi-momentum requires that  $\mathbf{q}'' = \mathbf{q} \pm \mathbf{q}' + \mathbf{Q}$  in the summation  $\sum^\pm$ , for some reciprocal lattice vector  $\mathbf{Q}$  such that  $\mathbf{q}''$  is in the same image of the

Brillouin zone as  $\mathbf{q}$  and  $\mathbf{q}'$ . The three-phonon scattering rates,  $\Gamma_{\lambda\lambda'\lambda''}^\pm$ , are computed as

$$\Gamma_{\lambda\lambda'\lambda''}^+ \equiv \frac{\hbar\pi}{4} \frac{f'_0 - f''_0}{\omega_\lambda \omega_{\lambda'} \omega_{\lambda''}} |V_{\lambda\lambda'\lambda''}^+|^2 \delta(\omega_\lambda + \omega_{\lambda'} - \omega_{\lambda''}), \quad (12)$$

and

$$\Gamma_{\lambda\lambda'\lambda''}^- \equiv \frac{\hbar\pi}{4} \frac{f'_0 + f''_0 + 1}{\omega_\lambda \omega_{\lambda'} \omega_{\lambda''}} |V_{\lambda\lambda'\lambda''}^-|^2 \delta(\omega_\lambda - \omega_{\lambda'} - \omega_{\lambda''}). \quad (13)$$

The scattering matrix elements,  $V_{\lambda\lambda'\lambda''}^\pm$ , are given by [49, 50]

$$V_{\lambda\lambda'\lambda''}^\pm = \sum_{\substack{i \in \text{uc} \\ \{j,k\} \in \text{sc} \\ \alpha\beta\gamma}} \Phi(i, j, k)_{\alpha\beta\gamma} \frac{e_\lambda^\alpha(i) e_{p', \pm \mathbf{q}'}^\beta(j) e_{p', -\mathbf{q}'}^\gamma(k)}{\sqrt{M(i)M(j)M(k)}}, \quad (14)$$

where  $\Phi(i, j, k)_{\alpha\beta\gamma}$  are the anharmonic force constants (introduced below) and  $e_{p', \pm \mathbf{q}'}^\beta(j)$  is the element of the eigenvector of branch  $p'$  at point  $\pm \mathbf{q}'$  that corresponds to  $j$ -atom in the  $\beta$ -direction. Note the indices  $\{i \in \text{uc (unit cell)}\}$  while  $\{j, k \in \text{sc (supercell)}\}$ . The conservation of energy, enforced by the Dirac distribution, can cause numerical instability during the calculations. Thus, we follow Li *et al.* [24] and substitute  $\delta$  with a normalized Gaussian distribution  $g$ :  $\delta(\dots) \rightarrow g(\dots)$  in Eqns. (12-13) with

$$\begin{aligned} g(\omega_\lambda - (\pm\omega_{\lambda'} + \omega_{\lambda''})) &\equiv \frac{1}{\sqrt{2\pi}\sigma} e^{-\frac{(\omega_\lambda - (\pm\omega_{\lambda'} + \omega_{\lambda''}))^2}{2\sigma^2}}, \\ \sigma &\equiv \zeta \sigma(\pm\omega_{\lambda'} + \omega_{\lambda''}) = \\ &= \frac{\zeta}{\sqrt{12}} \sqrt{\sum_\nu \left[ \sum_\alpha (v_{\lambda'}^\alpha - v_{\lambda''}^\alpha) \frac{Q_\nu^\alpha}{N_\nu} \right]^2}, \end{aligned} \quad (15)$$

where  $Q_\nu^\alpha$  is the component in the Cartesian direction,  $\alpha$ , of the reciprocal-space lattice vector  $\mathbf{Q}_\nu$  and  $N_\nu$  is the number of points of the  $\mathbf{q}$ -points grid in the reciprocal-space direction  $\nu$ . In principle, the parameter  $\zeta$  could be taken equal to one. However, it can be adjusted to lower values to increase the speed of the calculations, without much effect on the overall accuracy of the integrations.

**Interatomic Force Constants (IFCs).** The  $n^{\text{th}}$ -order interatomic force constants IFCs,  $\Phi(i, j, \dots)^{\alpha\beta\dots}$  are tensorial quantities representing derivatives of the potential energy ( $V$ ) with respect to the atomic displacements from equilibrium:

$$\begin{aligned} V &= V_0 + \frac{1}{2!} \sum_{ij, \alpha\beta} \Phi(i, j)_{\alpha\beta} r(i)^\alpha r(j)^\beta + \\ &+ \frac{1}{3!} \sum_{ijk, \alpha\beta\gamma} \Phi(i, j, k)_{\alpha\beta\gamma} r(i)^\alpha r(j)^\beta r(k)^\gamma + \dots \end{aligned} \quad (16)$$

Labels  $i, j, k, \dots$  span atoms of the cell and indices  $\alpha, \beta, \gamma, \dots$  are the Cartesian directions of the displacement. Second order harmonic IFC,  $\Phi(i, j)^{\alpha\beta}$ , calculations were already implemented in the original harmonic APL library [27] which obtains dispersion curves using three

different approaches: direct force constant [61–63], linear response and projector-augmented wave potentials [64], and the frozen phonon methods [65, 66].

Third order IFCs,  $\Phi(i, j, k)_{\alpha\beta\gamma}$  contain information about the anharmonicity of the lattice and they tend to rule phonon scattering in single crystals in the medium-temperature ranges [67, 68]. Given the choice of a supercell size, the finite difference method to calculate the third-order IFCs leads to:

$$\begin{aligned} \Phi(i, j, k)_{\alpha\beta\gamma} &\equiv \frac{\partial^3 V}{\partial r(i)^\alpha \partial r(j)^\beta \partial r(k)^\gamma} \simeq \\ &\simeq \frac{1}{2h} \left[ \frac{\partial^2 V}{\partial r(j)^\beta \partial r(k)^\gamma} (h(i)^\alpha) - \frac{\partial^2 V}{\partial h(j)^\beta \partial r(k)^\gamma} (-h(i)^\alpha) \right] \\ &\simeq \frac{1}{4h^2} \left[ -\psi(h(i)^\alpha, h(j)^\beta, k)_\gamma + \psi(-h(i)^\alpha, h(j)^\beta, k)_\gamma \right. \\ &\quad \left. + \psi(h(i)^\alpha, -h(j)^\beta, k)_\gamma - \psi(-h(i)^\alpha, -h(j)^\beta, k)_\gamma \right] \end{aligned} \quad (17)$$

where  $\{\pm h(i)^\alpha\}, \{\pm h(j)^\beta\}$  represent displacements of magnitude  $h$  of the  $i, j$ -atoms in the Cartesian directions  $\pm\alpha, \pm\beta$  and  $\psi(\pm h(i)^\alpha, \pm h(j)^\beta, k)_\gamma$  are the  $\gamma$ -components of the forces felt by the  $k$ -atom in the distorted configurations caused by the  $i$ - and  $j$ -atoms.

The third order IFCs' calculation is computationally intensive: each  $\Phi(i, j, k)_{\alpha\beta\gamma}$  requires four supercell calculations (Eq. 17). Effective use of crystal symmetry can help the process [69]. APL uses point, factor and space group symmetry operations computed by the AFLOW symmetry engine [25] to identify equivalence between single, pairs and triplets of atoms (positions) and test equivalence between other field quantities, such as differential  $\Phi$  or finite difference forces  $\psi$  (covariantly transforming). To avoid confusion, here we use indices as super  $\{\alpha\beta\gamma\dots\}$  or subscripts  $\{\alpha\beta\gamma\dots\}$  to identify the character of the symmetry transformation to be applied [70].

The reduction of third order IFC' calculations is performed through the following steps:

1) Inequivalent atoms, pairs and triplets are identified using space group symmetries. The user chooses the neighbor-shell cut-off and only pairs/triplets completely contained are considered.

2) The IFC tensors belonging to inequivalent triplets are analyzed. The symmetry operations mapping the representative inequivalent to the equivalent  $\Phi$  are saved:  $\Phi(i, j, k)_{\alpha\beta\gamma} \rightarrow \Phi'(i', j', k')_{\alpha'\beta'\gamma'}$ .

3) Each inequivalent tensor  $\Phi(i, j, k)_{\alpha\beta\gamma}$  contains  $3 \times 3 \times 3 = 27$  coefficients. Every static *ab-initio* calculation produces the vectorial force field for all the  $k$ -atoms of the supercell (where each  $k$ , combined with the inequivalent pair  $(i, j)$ , possibly generates  $(i, j, k)$  inequivalent triplets) starting from a combination of deformed positions for the  $i$ - and  $j$ -atoms belonging to inequivalent pairs. This requires the evaluation of  $3 \times 3 = 9$  configurations. Following Eq. (17) four forces  $\psi(\pm h(i)^\alpha, \pm h(j)^\beta, k)_\gamma$  are required for every entry  $\Phi(i, j, k)_{\alpha\beta\gamma}$ . To conclude, a total of 36 static calculations are necessary to parameterize

$\Phi(i, j, \forall k \in \text{sc})$ .

4) A large look-up table of all the necessary finite difference forces  $\psi(h(i)^\alpha, h(j)^\beta, k)$  is prepared at the beginning of the process. Every  $\psi$  can be constituent of many inequivalent  $\Phi(i, j, k)_{\alpha\beta\gamma}$ , and, within each  $\Phi$ , be a term in several internal coefficients. To exploit redundancy, the force field generated by every static *ab-initio* calculation is mapped through symmetry operations to recover as many possible other  $\psi(h(i)^\alpha, h(j)^\beta, \forall k \in \text{sc})_\gamma \rightarrow \psi(h(i')^{\alpha'}, h(j')^{\beta'}, \forall k' \in \text{sc})_{\gamma'}$ . Calculated and symmetry reproduced  $\psi$  are then removed from the table, and the algorithm moves to the next one to characterize. The process is repeated until all the  $\psi$  are found. The process guarantees that only the minimum amount of calculations are performed, compatible with the model of Eq. (17).

5) During the process, many equivalent entries of the tensors  $\Phi(i, j, k)_{\alpha\beta\gamma}$  are generated by the static *ab-initio* calculations. Because of unavoidable numerical noise, often equivalent entries have slightly different values, and the final value needs to be symmetrized somehow. This is performed during the re-symmetrization necessary to address the “sum rules” conservation.

**Sum rules and re-symmetrization.** Invariance with respect to any global rigid displacement translates into “sum rules” for anharmonic IFCs:

$$\sum_k \Phi(i, j, k)_{\alpha\beta\gamma} = 0, \quad \forall \text{ permutations of } i, j, k. \quad (18)$$

Due to finite size effects, the calculated IFCs are not perfectly symmetric and do not strictly satisfy Eqns. (18), causing numerical instabilities. To tackle the issue, we implement an iterative algorithm which corrects  $\Phi(i, j, k)$  and fulfills the constraints.

Given a set of  $\Phi(i, j, k)$  the error  $x$  of each sum rule at step  $\mathcal{N}$  is defined as:

$$x(i, j)_{\alpha\beta\gamma}^{\mathcal{N}} \equiv \sum_k \Phi(i, j, k)_{\alpha\beta\gamma}^{\mathcal{N}} \quad (19)$$

Each iteration is composed of correction and re-symmetrization of equivalent IFCs. Correction,  $\Phi(i, j, k)_{\alpha\beta\gamma}^{\mathcal{N}} \rightarrow \Phi(i, j, k)_{\alpha\beta\gamma}^{\mathcal{N}+1}$  is given by:

$$\begin{aligned} \Phi(i, j, k)_{\alpha\beta\gamma}^{\mathcal{N}+1} &= (1 - \mu) \Phi(i, j, k)_{\alpha\beta\gamma}^{\mathcal{N}} + \frac{\mu}{n_{\text{eq}}} \times \\ &\times \sum_{\substack{\text{eq} \\ i' j' k' \\ \alpha' \beta' \gamma'}} \left( \Phi(i', j', k')_{\alpha' \beta' \gamma'}^{\mathcal{N}} - \frac{x(i', j')_{\alpha' \beta' \gamma'}^{\mathcal{N}} |\Phi(i', j', k')_{\alpha' \beta' \gamma'}^{\mathcal{N}}|}{\sum_{k''} |\Phi(i', j', k'')_{\alpha' \beta' \gamma'}^{\mathcal{N}}|} \right), \end{aligned} \quad (20)$$

where the term  $x^{\mathcal{N}} |\Phi^{\mathcal{N}}| / \sum |\Phi^{\mathcal{N}}|$  corrects  $\Phi$  based on the total error times the absolute contribution of  $\Phi$  in the “sum rule”. The sum over the combination of indices  $\{i', j', k', \alpha', \beta', \gamma'\}$  giving IFCs equivalent to  $\Phi(i, j, k)_{\alpha\beta\gamma}$  (there are  $n_{\text{eq}}$ ) is meant to symmetrize the error across all the entries. The mixing fraction in the iterative process,  $\mu$ , can be adjusted by the user to optimize convergence rate and robustness. Overall, with increasing number

of neighbor shells, the user can effectively reduce this systematic error and achieve effective convergence of  $\kappa_l$ .

### Calculation workflows.

- Anharmonic scattering time  $\tau_\lambda^{\text{anh}}$ :

$$\begin{array}{c} \text{AFLOW-AAPL} \xrightarrow{\text{finite forces}} \psi \xrightarrow[\text{force constants}]{\text{Eq.(17)}} \Phi^{\mathcal{N}} \xrightarrow[\text{symmetrization}]{\text{Eq.(20)}} \Phi \rightarrow \\ \text{Eq.(14)} \xrightarrow{\text{scatt. matrix}} V^\pm \xrightarrow[\text{scatt. rates}]{\text{Eqns.(12-13)}} \Gamma^\pm \xrightarrow[\text{anh. scatt. time}]{\text{Eq.(11)}} \tau_\lambda^{\text{anh}}. \end{array} \quad (21)$$

- Elastic scattering time  $\tau_\lambda^{\text{iso}}$  (isotopic disorder) and grain boundaries scattering time  $\tau_\lambda^{\text{bnd}}$  (polycrystalline materials):

$$\begin{array}{c} \text{AFLOW-AAPL} \xrightarrow{\text{ab initio}} \psi \xrightarrow[\text{force const.}]{\text{Eq.(16)}} \Phi \xrightarrow[\text{dynamical mat.}]{\text{Eq.(4)}} D(\mathbf{q}) \rightarrow \\ \left\{ \begin{array}{l} \text{Eq.(3)} \rightarrow \omega_\lambda \xrightarrow[\text{elastic scatt. time, rate}]{\text{Eq.(8)}} \tau_\lambda^{\text{iso}}, \Gamma_{\lambda\lambda'} \\ \text{Eq.(6)} \rightarrow v_\lambda \xrightarrow[\text{grain bound. scatt. time}]{\text{Eq.(9)}} \tau_\lambda^{\text{bnd}}. \end{array} \right. \end{array} \quad (22)$$

- Conductivity  $\kappa_l^{\alpha\beta}$ :

$$\begin{array}{c} \{\tau_\lambda^{\text{anh}}, \tau_\lambda^{\text{iso}}, \tau_\lambda^{\text{bnd}}\} \xrightarrow[\text{total scatt. time}]{\text{Eq.(7)}} \tau_\lambda^0 \rightarrow \\ \xrightarrow[\text{mean free disp.}]{\text{Eq.(2)}} \mathbf{F}_\lambda \xrightarrow[\text{conductivity}]{\text{Eq.(1)}} \kappa_l^{\alpha\beta}. \end{array} \quad (23)$$

## III. COMPUTATIONAL DETAILS

**Geometry optimization.** All structures are fully relaxed using the automated framework AFLOW [27–35] and the VASP package [71]. Optimizations are performed following the AFLOW standards [31]. We use the projector augmented wave (PAW) potentials [72] and the exchange and correlation functionals parameterized by the generalized gradient approximation proposed by Perdew-Burke-Ernzerhof (PBE) [73]. All calculations use a high energy-cut-off, which is 40% larger than the maximum recommended cut-off among all component potentials, and a  $\mathbf{k}$ -point mesh of 8,000  $\mathbf{k}$ -points per reciprocal atom. Primitive cells are fully relaxed (lattice parameters and ionic positions) until the energy difference between two consecutive ionic steps is smaller than  $10^{-4}$  eV and forces in each atom are below  $10^{-3}$  eV/Å.

**Phonon calculations.** Phonon calculations are performed out using the automatic phonon library, APL, as implemented in AFLOW, and by using VASP to obtain the 2<sup>nd</sup> order IFCs via the finite-displacement approach [74]. The magnitude of the displacement is 0.015 Å. Electronic self consistent field (SCF) iterations for static calculations are stopped when the difference of energy between the last two steps is less than  $10^{-5}$  meV. The threshold ensures a good convergence for the wavefunction and sufficiently accurate values for forces and harmonic constants. Non-analytic contributions to the dynamical matrix are also

included using the formulation developed by Wang *et al.* [54]. Frequencies and other related phonon properties are calculated on a  $21 \times 21 \times 21$   $\mathbf{q}$ -point mesh in the Brillouin zone, which is a tradeoff between the computational load, convergence of the phonon density of states, pDOS, and the derived thermodynamic properties. Integrations within the Brillouin zone are obtained by using the linear interpolation tetrahedron method available in AFLOW.

**Lattice thermal conductivity.** Anharmonic force constants are extracted from a  $4 \times 4 \times 4$  supercell using a cut-off that includes all 4<sup>th</sup> neighbor shells. Thermal conductivity is evaluated on a  $21 \times 21 \times 21$   $\mathbf{q}$ -point mesh using  $\zeta = 0.1$  for the Gaussian smoothing, Eq. (15). The dense mesh ensures the convergence of the values obtained for  $\kappa_l$  [24]. The IFCs' calculations are iterated self-consistently until all sum rules are smaller  $10^{-7}$  eV/Å<sup>3</sup>.

**Analysis of Results.** Different statistical parameters are used to measure the qualitative and quantitative agreement of AAPL with respect to experimental values. The Pearson correlation coefficient  $r[\{X\}, \{Y\}]$  is a measure of the linear correlation between two variables,  $\{X\}$  and  $\{Y\}$ :

$$r = \frac{\sum_i (X_i - \bar{X})(Y_i - \bar{Y})}{\sqrt{\sum_i (X_i - \bar{X})^2} \sqrt{\sum_i (Y_i - \bar{Y})^2}}, \quad (24)$$

where  $\bar{X}$  and  $\bar{Y}$  are the averages of  $\{X\}$  and  $\{Y\}$ .

The Spearman rank correlation coefficient  $\rho[\{X\}, \{Y\}]$  is a measure of the monotonicity of the relationship between two variables. The values of the two variables  $\{X\}$  and  $\{Y\}$  are sorted in ascending order, and are assigned rank values  $\{x\}$  and  $\{y\}$  which are equal to their position in the sorted list. The correlation coefficient is then given by

$$\rho = \frac{\sum_i (x_i - \bar{x})(y_i - \bar{y})}{\sqrt{\sum_i (x_i - \bar{x})^2} \sqrt{\sum_i (y_i - \bar{y})^2}}. \quad (25)$$

$\rho$  is useful for determining how well the values of one variable can predict the ranking of the other variable.

We also investigate the root-mean-square relative deviation, RMSrD, of the calculated  $\kappa$  *versus* the experiment. The RMSrD will measure the quantitative difference between AAPL and experimental results:

$$\text{RMSrD} = \sqrt{\frac{\sum_i \left(\frac{X_i - Y_i}{X_i}\right)^2}{N_{\{X, Y\}} - 1}}, \quad (26)$$

Lower values of RMSrD indicate better agreement.

## IV. RESULTS

**Scaling.** The calculation of the anharmonic IFCs is the most computationally expensive step in the method.

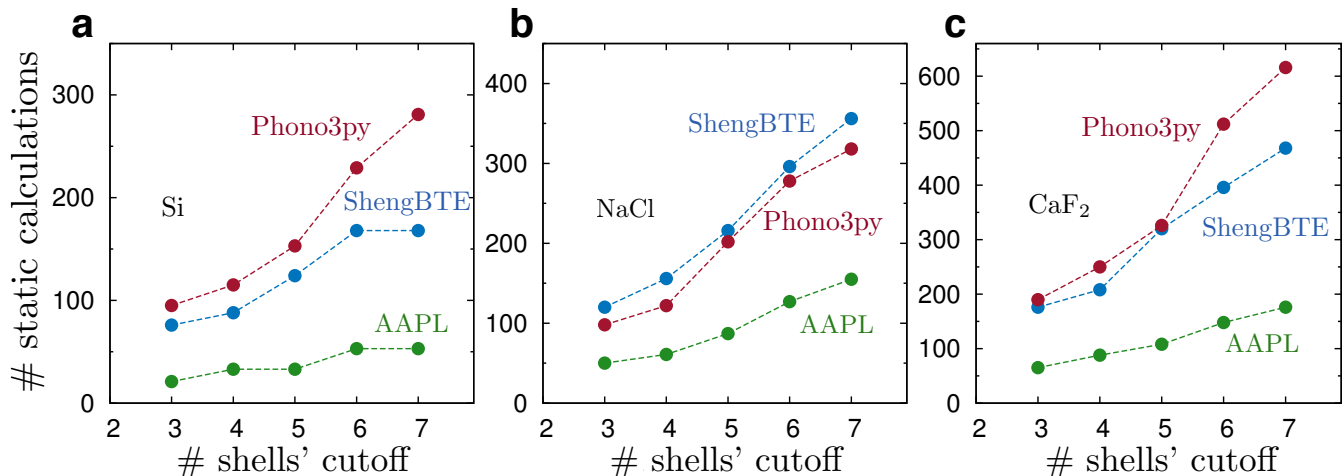


FIG. 1. Number of required static calculations for (a) Si, (b) NaCl, and (c) CaF<sub>2</sub> for the computation of the 3rd order IFCs, applying different cut-offs ( $n^{\text{th}}$  neighbor) using AACL (green), Phono3py (red), and ShengBTE (blue).

First, we test the number of required calculations for some structural prototypes such as diamond (spacegroup:  $Fd\bar{3}m$ , #227; Pearson symbol:  $cF8$ ; *Strukturbericht* designation: A4; AFLOW Prototype: A\_cF8\_227\_a [25]), rock-salt ( $Fm\bar{3}m$ , #225,  $cF8$ , B1, AB\_cF8\_225\_a-b [25]) and fluorite ( $Fm\bar{3}m$ , #225,  $cF12$ , C1, AB2\_cF12\_225\_a-c [25]) for which there are abundant available experimental data. We compare the number of calculations and how they scale with respect to the chosen cut-off for the IFCs (see Figure 1) for different available software (Phono3py and ShengBTE software packages). The number of required static calculations increases with the cell's complexity, the total number of atoms, and the number of inequivalent positions in the primitive cell. AACL reduces the number of required calculations compared to the other two codes for the three tested prototypes, indicating that the AACL algorithm is efficient at handling symmetry equivalence. For example, in silicon and using the minimum shell cut-off, AACL only needs 21 calculations, while ShengBTE requires 76. The advantage is preserved while increasing the range of the interactions. For example, Phono3py requires 616 static calculations for CaF<sub>2</sub> with 7<sup>th</sup> neighbor shells, whereas AACL needs less than one third of this amount (176). Figure 1 summarizes the scaling results.

**Validation with experiments.** A data set of 30 compounds is used to validate our framework. The list of materials includes semiconductors and insulators that belong to different structural prototypes such as diamond (A\_cF8\_227\_a [25]), rock-salt (AB\_cF8\_225\_a-b [25]), and fluorite (AB2\_cF12\_225\_a-c [25]). To maximize the heterogeneity of the data set, we select materials containing as many different elements as possible from the  $s$ -,  $p$ -, and  $d$ -blocks of the periodic table. The comparison of calculated *versus* experimental values of  $\kappa_l$  is summarized in Table I and Figure 2.

We use different statistical quantities to measure qualitative and quantitative agreement between the AACL and experimental results (Table II). AACL results strongly correlate with experimental findings, with relatively small

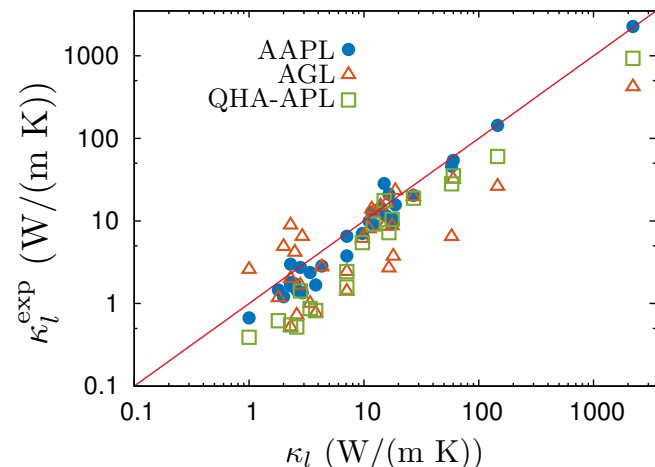


FIG. 2. Calculated lattice thermal conductivities at 300 K *versus* experimental. Blue circles are used for AACL results, empty orange triangles for the quick AFLOW-AGL prediction of Refs. [14, 28], and empty green squares for AFLOW-QHA-APL results of Ref. [6]. The red line represents equality (calculation=experiments).

RMSrD from experiment demonstrating the reliability and robustness of the framework. The algorithm should not be blamed for systematic errors in the *ab-initio* characterization of the compounds (such as the ones containing Pb).

We also compare AACL with approximate phenomenological frameworks such as AFLOW-AGL [14] and AFLOW-QHA-APL [6, 74]. Qualitatively, all three frameworks have high linear correlation with experiments (Pearson,  $r$ ); AACL and QHA-APL are also very effective in rank ordering the compounds (Spearman,  $\rho$ ). Quantitatively, AACL has the lowest RMSrD value, followed by QHA-APL and AGL. Accuracy strongly correlates with computational costs (AACL  $\gg$  QHA-APL  $>$  AGL), so that the users can choose which technique best fulfills their screening needs.

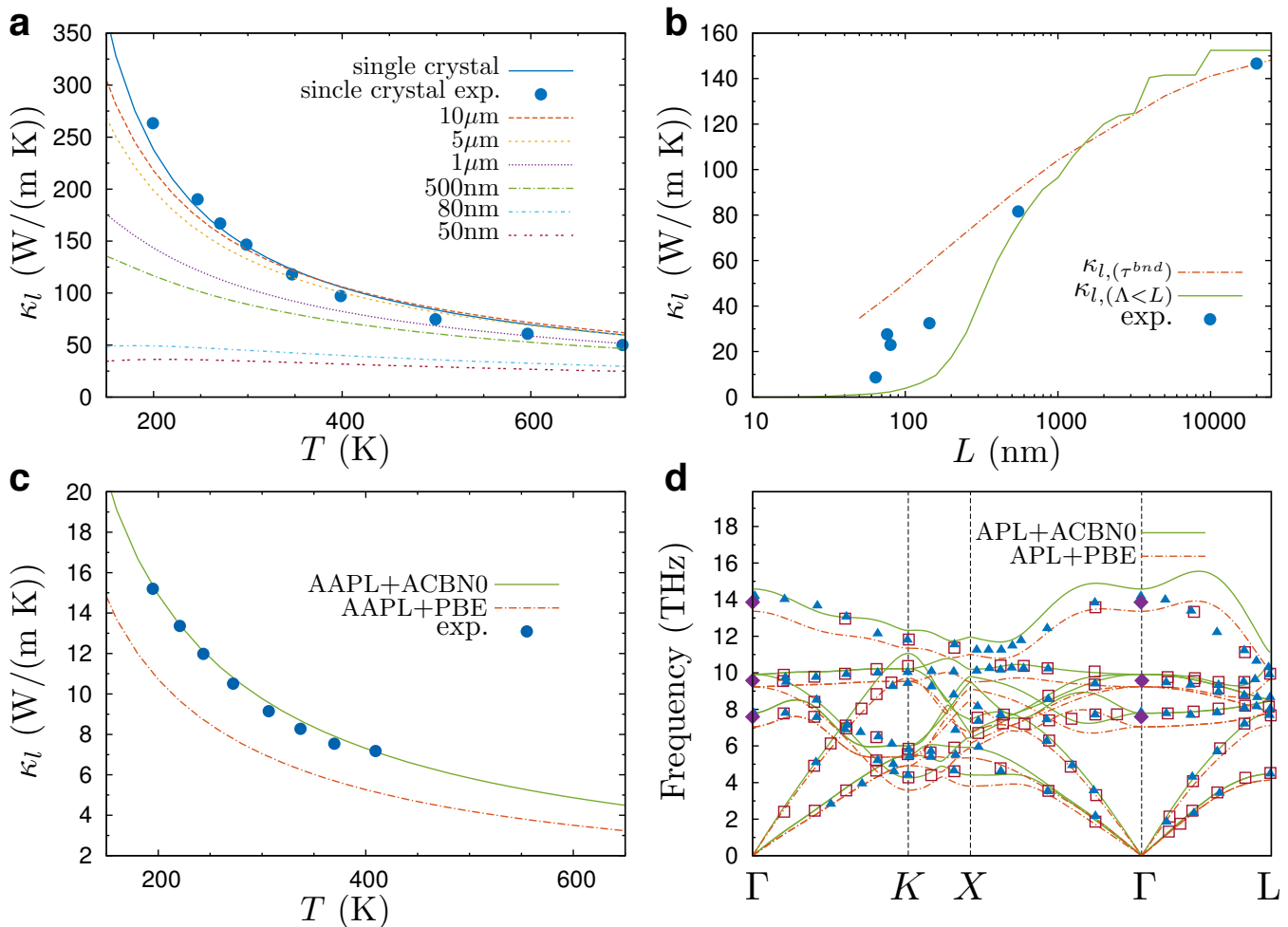


FIG. 3. (a) Calculated lattice thermal conductivity for single-crystal (blue) and nanocrystalline silicon with different grain size. Blue circles represent measurements for single-crystal Si from Ref. [77]. (b) Cumulative lattice thermal conductivity,  $\kappa_{l,(\Lambda < L)}$ , (green) of Si as a function of the average grain size,  $L$ , at 300 K. Lattice thermal conductivity (orange) including the scattering of phonons due to grain boundaries (see Eq. 9) is also presented. Blue circles represent experimental data from Ref. [85]. (c) Lattice thermal conductivity of  $\text{CaF}_2$  within the ACBN0 method (green) and PBE functional (orange). Blue circles represent experimental data from Ref. [86]. (d) Phonon dispersion of  $\text{CaF}_2$  within the ACBN0 method (green). The PBE phonon dispersion (orange) is also shown for comparison. Blue triangles and open squares represent neutron scattering data from Ref. [87] and Ref. [88] respectively. Purple diamonds represent Raman and infrared data from Ref. [89].

**Single-crystal and nanocrystalline silicon.** Silicon is the perfect benchmark for testing the reliability of AAPL: extensive availability of experimental data for well characterized samples [77, 85] and limited computational cost due to the diamond crystal structure with two atoms in the primitive cell and fcc lattice. Figure 3(a) depicts the calculated lattice thermal conductivity at different temperatures for single-crystal and polycrystalline samples compared to single-crystal experimental values from Ref. [77]. Boundary effects can be included in two ways: **i.** by calculating the complete  $\kappa_l^{\alpha\beta}(L)$  (workflow (23)) for average grain sizes having different  $\tau_{\lambda}^{\text{bnd}}(L)$  (Workflow (22)) or **ii.** by neglecting  $\tau^{\text{bnd}}$  from the total scattering time  $\tau_{\lambda}^0$  (Eq. (7)) and restricting the summation to the modes with a mean free path shorter than  $L$  ( $\Lambda < L$ , Eq. (10)):  $\kappa_{l,(\Lambda < L)}^{\alpha\beta}$ . Both approaches are implemented in AAPL. Comparison with experimental val-

ues for different polycrystalline Si samples (average grain size  $L=64, 76, 80, 155, 550$  and  $20000$  nm) at 300 K are presented in Figure 3(b). Both approximations of grain boundary scattering effects show the same trend and are very close to the experimental results, corroborating the validity of our approaches.

#### Extension to ACBN0 pseudo-hybrid functional.

The accuracy of the results ultimately relies on the quality of the computed IFCs with *ab-initio*. The use of hybrid functionals [90] or advanced electronic structure methods such as *GW* [91] to compute the IFCs is limited [92, 93] because of their computational costs. Recently, the ACBN0 functional was introduced in order to facilitate the accurate characterization of electronic properties of correlated materials [37]. ACBN0 is a pseudo-hybrid Hubbard density functional that introduces a new self-consistent *ab-initio* approach to compute  $U$  without the need for

TABLE I. Calculated and experimental lattice thermal conductivity of diamond (Strukturbericht: A4; AFLOW standardized prototype name A\_cF8\_227\_a [25]), rocksalt (B1, AB\_cF8\_225\_a\_b [25]) and fluorite (C1, AB2\_cF12\_225\_a\_c [25]) structure semiconductors and insulators at 300 K. Units:  $\kappa_l$  in W/(m K).

Formula	Pearson	s.g.#	Struk. <sup>a</sup>	$\kappa_l^{\text{AAPL}}$	$\kappa_l^{\text{Exp}}$
C	<i>cF8</i>	227	A4	2270 2200 [75, 76]	
Si	<i>cF8</i>	227	A4	144	146 [77]
Ge	<i>cF8</i>	227	A4	46.17	58 [78]
AgCl	<i>cF8</i>	225	B1	0.67	1 [79]
BaO	<i>cF8</i>	225	B1	2.99	2.3 [79]
CaO	<i>cF8</i>	225	B1	20.41	27 [79]
KBr	<i>cF8</i>	225	B1	2.38	3.4 [79]
KCl	<i>cF8</i>	225	B1	3.77	7.1 [79]
KI	<i>cF8</i>	225	B1	1.46	2.6 [79]
LiF	<i>cF8</i>	225	B1	10.73	17.6 [79]
LiH	<i>cF8</i>	225	B1	28.4	15 [79]
MgO	<i>cF8</i>	225	B1	54.06	60 [79]
NaBr	<i>cF8</i>	225	B1	2.74	2.8 [79]
NaCl	<i>cF8</i>	225	B1	6.53	7.1 [79]
NaF	<i>cF8</i>	225	B1	21.11	16.5 [79]
NaI	<i>cF8</i>	225	B1	1.46	1.8 [79]
PbS	<i>cF8</i>	225	B1	1.35	2.9 [79]
PbSe	<i>cF8</i>	225	B1	1.21	2.0 [79]
PbTe	<i>cF8</i>	225	B1	1.73	2.5 [79]
RbBr	<i>cF8</i>	225	B1	1.68	3.8 [79]
RbI	<i>cF8</i>	225	B1	1.64	2.3 [79]
SrO	<i>cF8</i>	225	B1	9.12	12 [79]
CdF <sub>2</sub>	<i>cF12</i>	225	C1	3.01	4.30 [80]
SrCl <sub>2</sub>	<i>cF12</i>	225	C1	1.80	2.3 [81]
Mg <sub>2</sub> Si	<i>cF12</i>	225	C1	15.67	18.8 <sup>b</sup> [82]
Mg <sub>2</sub> Ge	<i>cF12</i>	225	C1	11.49	15.7 <sup>b</sup> [82]
Mg <sub>2</sub> Sn	<i>cF12</i>	225	C1	9.91	11.1 <sup>b</sup> [82]
Mg <sub>2</sub> Pb	<i>cF12</i>	225	C1	9.20	18 <sup>b</sup> [82]
CaF <sub>2</sub>	<i>cF12</i>	225	C1	7.04	9.76 [80]
CeO <sub>2</sub>	<i>cF12</i>	225	C1	11.35	10.8 [83]
ThO <sub>2</sub>	<i>cF12</i>	225	C1	14.42	14 [84]

<sup>a</sup> Strukturbericht

<sup>b</sup>  $\kappa_l$  at 200 K

TABLE II. Root mean square relative deviation (RMSrD), and Pearson and Spearman correlation for the material data set.

	AGL	QHA-APL	AAPL
$r$	0.997	0.999	0.999
$\rho$	0.706	0.976	0.933
RMSrD	86.20%	58.16%	27.57%

empirical parameters. ACBN0 can improve not only the description of the electronic structure, but also the prediction of the structural and the vibrational parameters of solids [42]. One of the reasons for this is the better prediction of the Born charges,  $\mathbf{Z}$ , and the dielectric tensor,  $\epsilon_\infty$ , compared to LDA or GGA functionals [42]. If the ACBN0 functional improves the vibrational parameters of solids, we can assume that the calculations of other temperature-dependent properties such as  $\kappa_l$  may be improved too. As

a testbed, we chose calcium fluoride, CaF<sub>2</sub>, because of the ample available experimental data [80, 87–89]. CaF<sub>2</sub> has been extensively used in optical devices due to its low refractive index, wide band gap, low dispersion, and large broadband radiation transmittance [94–96].

We use the package AFLOW $\pi$  [97] to obtain the ACBN0 electronic structure of CaF<sub>2</sub>. We obtain  $U_{\text{eff}}$  of 13.43 for F- $p$  orbitals. We then use this value inside AAPL for the rest of the calculations. AAPL+ACBN0 almost perfectly predicts the experimental  $\kappa_l$  in contrast with AAPL+PBE which greatly underestimates  $\kappa_l$  over the entire temperature range (Figure 3(c)). Phonon band structures have also been calculated with the harmonic library (APL) to explain the difference (Figure 3(d)). ACBN0 reproduces the phonon dispersion better than the PBE functional. PBE, as a GGA functional, overestimates bond length and hence it tends to underestimate vibrational frequencies [98]. On the contrary, ACBN0 describes the bond length more accurately, obtaining frequencies higher than PBE and closer to the experimental values [87]. Major differences between ACBN0 and PBE results come from the optical bands, so we compared the two main properties that are involved in the splitting of the optical band due to the non-analytical contributions to the dynamical matrix. While the Born charges are similar for ACBN0 and PBE (2.33 e and 2.34 e respectively), there are significant differences in the high-frequency dielectric constant  $\epsilon_\infty$  (2.083 and 2.305 respectively). The value obtained using ACBN0 is closer to the experimental  $\epsilon_\infty$  (2.045) [89] than that obtained using PBE.

## V. CONCLUSIONS

The Automatic-Anharmonic-Phonon-Library, AAPL, was developed to compute the third order IFCs and solve the BTE within the high-throughput AFLOW framework. This code automatically predicts the lattice thermal conductivity of single-crystals and polycrystalline materials using a single input file and with no further user intervention. The symmetry analysis has been optimized to further reduce the number of static calculations compared to other packages. The robustness and accuracy of the code have been tested with a set of 30 materials that belong to different space groups. APL has been combined with the ACBN0 pseudo-hybrid functional to predict the lattice thermal conductivity of CaF<sub>2</sub>. Our results demonstrate that using ACBN0 can improve not only the electronic structure description of the material compared to the GGA functional, but also phonon-dependent properties such as the thermal conductivity.

## VI. ACRONYMS IN THE AFLOW PACKAGE

AAPL: Automatic-Anharmonic-Phonon-Library; AGL: AFLOW-Gibbs-Library [14]; APL: Automatic-Phonon-Library [27, 32]; AEL: AFLOW-Elastic-Library [15]; QHA: quasiharmonic approximation [6]; ACBN0: Agapito

Curtarolo Buongiorno Nardelli *ab-initio* DFT functional [37]; AFLOW $\pi$ : A minimalist AFLOW-Python approach to high-throughput *ab initio* calculations including the generation of tight-binding hamiltonians and the calculation of the ACBN0 functional [97].

## VII. ACKNOWLEDGEMENTS

We thank Drs. Kristin Persson, Gerbrand Ceder, Natalio Mingo, David Hicks, Mike Mehl, Ohad Levy, and Corey Oses for various technical discussions. We acknowledge support by the DOE (DE-AC02-05CH11231), specifically the Basic Energy Sciences program under Grant # EDCBEE. C.T., M.F., M.B.N. and S.C. acknowledge partial support by DOD-ONR (N00014-13-1-0635, N00014-11-1-0136, N00014-15-1-2863). The AFLOW consortium acknowledges Duke University – Center for Materials Genomics — and the CRAY corporation for computational support.

- 
- [1] M. Zebarjadi, K. Esfarjani, M. S. Dresselhaus, Z. F. Ren, and G. Chen, *Perspectives on thermoelectrics: from fundamentals to device applications*, Energy Environ. Sci. **5**, 5147–5162 (2012).
- [2] J. Carrete, W. Li, N. Mingo, S. Wang, and S. Curtarolo, *Finding Unprecedentedly Low-Thermal-Conductivity Half-Heusler Semiconductors via High-Throughput Materials Modeling*, Phys. Rev. X **4**, 011019 (2014).
- [3] L.-T. Yeh and R. C. Chu, *Thermal Management of Microelectronic Equipment: Heat Transfer Theory, Analysis Methods, and Design Practices* (ASME Press, 2002).
- [4] C. D. Wright, L. Wang, P. Shah, M. M. Aziz, E. Varesi, R. Bez, M. Moroni, and F. Cazzaniga, *The design of rewritable ultrahigh density scanning-probe phase-change memories*, IEEE Trans. Nanotechnol. **10**, 900–912 (2011).
- [5] D. G. Cahill, P. V. Braun, G. Chen, D. R. Clarke, S. Fan, K. E. Goodson, P. Keblinski, W. P. King, G. D. Mahan, A. Majumdar, H. J. Maris, S. R. Phillpot, E. Pop, and L. Shi, *Nanoscale thermal transport. II. 2003-2012*, Appl. Phys. Rev. **1**, 011305 (2014).
- [6] P. Nath, J. J. Plata, D. Usanmaz, C. Toher, M. Fornari, M. Buongiorno Nardelli, and S. Curtarolo, *High Throughput combinatorial method for fast and robust prediction of lattice thermal conductivity*, Scr. Mater. (2016).
- [7] J. Ziman, *Electrons and phonons: The theory of transport phenomena in solids*. (Clarendon, 1960).
- [8] J. Callaway, *Model for Lattice Thermal Conductivity at Low Temperatures*, Phys. Rev. **113**, 1046–1051 (1959).
- [9] P. B. Allen, *Zero-point and isotope shifts: Relation to thermal shifts*, Phil. Mag. B **70**, 527–534 (1994).
- [10] M. S. Green, *Markoff random processes and the statistical mechanics of time-dependent phenomena. II. Irreversible processes in fluids*, J. Chem. Phys. **22**, 398–413 (1954).
- [11] R. Kubo, *Statistical-mechanical theory of irreversible processes. I. General theory and simple applications to magnetic and conduction problems*, J. Phys. Soc. Jpn. **12**, 570–586 (1957).
- [12] S. Curtarolo and G. Ceder, *Dynamics of an Inhomogeneously Coarse Grained Multiscale System*, Phys. Rev. Lett. **88**, 255504 (2002).
- [13] M. A. Blanco, E. Francisco, and V. Luaña, *GIBBS: isothermal-isobaric thermodynamics of solids from energy curves using a quasi-harmonic Debye model*, Comput. Phys. Commun. **158**, 57–72 (2004).
- [14] C. Toher, J. J. Plata, O. Levy, M. de Jong, M. D. Asta, M. Buongiorno Nardelli, and S. Curtarolo, *High-Throughput Computational Screening of thermal conductivity, Debye temperature and Grüneisen parameter using a quasi-harmonic Debye Model*, Phys. Rev. B **90**, 174107 (2014).
- [15] C. Toher, C. Oses, J. J. Plata, D. Hicks, F. Rose, O. Levy, M. de Jong, M. D. Asta, M. Buongiorno Nardelli, and S. Curtarolo, *Combining the AFLOW GIBBS and Elastic Libraries for efficiently and robustly screening thermo-mechanical properties of solids*, submitted (2016).
- [16] L. Bjerg, B. B. Iversen, and G. K. H. Madsen, *Modeling the thermal conductivities of the zinc antimonides ZnSb and Zn<sub>4</sub>Sb<sub>3</sub>*, Phys. Rev. B **89**, 0243041 (2014).
- [17] N. Mingo, D. A. Stewart, D. A. Broido, L. Lindsay, and W. Li, *Ab Initio Thermal Transport*, in *Length-Scale Dependent Phonon Interactions* (Springer New York, 2014), pp. 137–173.
- [18] D. A. Broido, M. Malorny, G. Birner, N. Mingo, and D. A. Stewart, *Intrinsic lattice thermal conductivity of semiconductors from first principles*, Appl. Phys. Lett. **91**, 231922 (2007).
- [19] A. Ward and D. A. Broido, *Intrinsic phonon relaxation times from first-principles studies of the thermal conductivities of Si and Ge*, Phys. Rev. B **81**, 085205 (2010).
- [20] X. Tang and J. Dong, *Lattice thermal conductivity of MgO at conditions of Earth’s interior*, Proc. Natl. Acad. Sci. **107**, 4539–4543 (2010).
- [21] A. Togo, L. Chaput, and I. Tanaka, *Distributions of phonon lifetimes in Brillouin zones*, Phys. Rev. B **91**, 094306 (2015).
- [22] A. Chernatynskiy and S. R. Phillpot, *Phonon Transport Simulator (PhonTS)*, Comput. Phys. Commun. **192**, 196–204 (2015).
- [23] T. Tadano, Y. Gohda, and S. Tsuneyuki, *Anharmonic force constants extracted from first-principles molecular dynamics: applications to heat transfer simulations*, J. Phys.: Condens. Matter **26**, 225402 (2014).
- [24] W. Li, J. Carrete, N. A. Katcho, and N. Mingo, *Sheng-BTE: A solver of the Boltzmann transport equation for phonons*, Comput. Phys. Commun. **185**, 1747–1758 (2014).
- [25] M. J. Mehl, D. Hicks, C. Toher, O. Levy, R. M. Hanson, G. L. W. Hart, and S. Curtarolo, *The AFLOW Library of Crystallographic Prototypes*, submitted (2016).
- [26] F. Zhou, W. Nielson, Y. Xia, and V. Ozoliņš, *Lattice Anharmonicity and Thermal Conductivity from Compressive Sensing of First-Principles Calculations*, Phys. Rev. Lett.

- 113**, 185501 (2014).
- [27] S. Curtarolo, W. Setyawan, G. L. W. Hart, M. Jahnátek, R. V. Chepulskii, R. H. Taylor, S. Wang, J. Xue, K. Yang, O. Levy, M. J. Mehl, H. T. Stokes, D. O. Demchenko, and D. Morgan, *AFLOW: an automatic framework for high-throughput materials discovery*, *Comput. Mater. Sci.* **58**, 218–226 (2012).
- [28] S. Curtarolo, W. Setyawan, S. Wang, J. Xue, K. Yang, R. H. Taylor, L. J. Nelson, G. L. W. Hart, S. Sanvito, M. Buongiorno Nardelli, N. Mingo, and O. Levy, *AFLOWLIB.ORG: A distributed materials properties repository from high-throughput ab initio calculations*, *Comput. Mater. Sci.* **58**, 227–235 (2012).
- [29] W. Setyawan and S. Curtarolo, *High-throughput electronic band structure calculations: Challenges and tools*, *Comput. Mater. Sci.* **49**, 299–312 (2010).
- [30] R. H. Taylor, F. Rose, C. Toher, O. Levy, K. Yang, M. Buongiorno Nardelli, and S. Curtarolo, *A RESTful API for exchanging Materials Data in the AFLOWLIB.org consortium*, *Comput. Mater. Sci.* **93**, 178–192 (2014).
- [31] C. E. Calderon, J. J. Plata, C. Toher, C. Osés, O. Levy, M. Fornari, A. Natan, M. J. Mehl, G. L. W. Hart, M. Buongiorno Nardelli, and S. Curtarolo, *The AFLOW standard for high-throughput materials science calculations*, *Comput. Mater. Sci.* **108 Part A**, 233–238 (2015).
- [32] O. Levy, M. Jahnátek, R. V. Chepulskii, G. L. W. Hart, and S. Curtarolo, *Ordered Structures in Rhenium Binary Alloys from First-Principles Calculations*, *J. Am. Chem. Soc.* **133**, 158–163 (2011).
- [33] O. Levy, G. L. W. Hart, and S. Curtarolo, *Structure maps for hcp metals from first-principles calculations*, *Phys. Rev. B* **81**, 174106 (2010).
- [34] O. Levy, G. L. W. Hart, and S. Curtarolo, *Uncovering Compounds by Synergy of Cluster Expansion and High-Throughput Methods*, *J. Am. Chem. Soc.* **132**, 4830–4833 (2010).
- [35] G. L. W. Hart, S. Curtarolo, T. B. Massalski, and O. Levy, *Comprehensive Search for New Phases and Compounds in Binary Alloy Systems Based on Platinum-Group Metals, Using a Computational First-Principles Approach*, *Phys. Rev. X* **3**, 041035 (2013).
- [36] A. Jain, S. P. Ong, G. Hautier, W. Chen, W. D. Richards, S. Dacek, S. Cholia, D. Gunter, D. Skinner, G. Ceder, and K. A. Persson, *Commentary: The Materials Project: A materials genome approach to accelerating materials innovation*, *APL Mater.* **1**, 011002 (2013).
- [37] L. A. Agapito, S. Curtarolo, and M. Buongiorno Nardelli, *Reformulation of DFT + U as a Pseudohybrid Hubbard Density Functional for Accelerated Materials Discovery*, *Phys. Rev. X* **5**, 011006 (2015).
- [38] P. D’Amico, L. A. Agapito, A. Catellani, A. Ruini, S. Curtarolo, M. Fornari, M. Buongiorno Nardelli, and A. Calzolari, *Accurate ab initio tight-binding Hamiltonians: Effective tools for electronic transport and optical spectroscopy from first principles*, *Phys. Rev. B* **94**, 165166 (2016).
- [39] L. A. Agapito, M. Fornari, D. Ceresoli, A. Ferretti, S. Curtarolo, and M. Buongiorno Nardelli, *Accurate Tight-Binding Hamiltonians for 2D and Layered Materials*, *Phys. Rev. B* **93**, 125137 (2016).
- [40] L. A. Agapito, S. Ismail-Beigi, S. Curtarolo, M. Fornari, and M. Buongiorno Nardelli, *Accurate tight-binding Hamiltonian matrices from ab initio calculations: Minimal basis sets*, *Phys. Rev. B* **93**, 035104 (2016).
- [41] Y. Tang, Z. M. GIBBS, L. A. Agapito, G. Li, H.-S. Kim, M. Buongiorno-Nardelli, S. Curtarolo, and G. J. Snyder, *Convergence of multi-valley bands as the electronic origin of high thermoelectric performance in CoSb<sub>3</sub> skutterudites*, *Nat. Mater.* **14**, 1223–1228 (2015).
- [42] P. Gopal, M. Fornari, S. Curtarolo, L. A. Agapito, L. S. I. Liyanage, and M. Buongiorno Nardelli, *Improved predictions of the physical properties of Zn- and Cd-based wide band-gap semiconductors: A validation of the ACBN0 functional*, *Phys. Rev. B* **91**, 245202 (2015).
- [43] L. A. Agapito, A. Ferretti, A. Calzolari, S. Curtarolo, and M. Buongiorno Nardelli, *Effective and accurate representation of extended Bloch states on finite Hilbert spaces*, *Phys. Rev. B* **88**, 165127 (2013).
- [44] P. B. Allen, *Improved Callaway model for lattice thermal conductivity*, *Phys. Rev. B* **88**, 144302 (2013).
- [45] G. Deinzer, G. Birner, and D. Strauch, *Ab initio calculation of the linewidth of various phonon modes in germanium and silicon*, *Phys. Rev. B* **67**, 1443041 (2003).
- [46] M. Omini and A. Sparavigna, *An iterative approach to the phonon Boltzmann equation in the theory of thermal conductivity*, *Physica B* **212**, 101–112 (1995).
- [47] M. Omini and A. Sparavigna, *Beyond the isotropic-model approximation in the theory of thermal conductivity*, *Phys. Rev. B* **53**, 9064–9073 (1996).
- [48] M. Omini and A. Sparavigna, *Heat transport in dielectric solids with diamond structure*, *Nuovo Cimento D* **19**, 1537–1563 (1997).
- [49] A. Ward, D. A. Broido, D. A. Stewart, and G. Deinzer, *Ab initio theory of the lattice thermal conductivity in diamond*, *Phys. Rev. B* **80**, 125203 (2009).
- [50] L. Lindsay and D. A. Broido, *Three-phonon phase space and lattice thermal conductivity in semiconductors*, *J. Phys.: Condens. Matter* **20**, 165209 (2008).
- [51] D. C. Wallace, *Thermodynamics of crystals* (John Wiley & Sons, 1972).
- [52] M. T. Dove, *Introduction to Lattice Dynamics* (Cambridge University Press, 1993).
- [53] G. P. Srivastava, *The Physics of Phonons* (CRC Press, Taylor & Francis, 1990).
- [54] Y. Wang, J. J. Wang, W. Y. Wang, Z. G. Mei, S. L. Shang, L. Q. Chen, and Z. K. Liu, *A mixed-space approach to first-principles calculations of phonon frequencies for polar materials*, *J. Phys.: Condens. Matter* **22**, 202201 (2010).
- [55] S. Baroni, S. de Gironcoli, A. D. Corso, and P. Gianozzi, *Phonons and related crystal properties from density-functional perturbation theory*, *Rev. Mod. Phys.* **73**, 515 (2001).
- [56] S. Tamura, *Isotope scattering of dispersive phonons in Ge*, *Phys. Rev. B* **27**, 858–866 (1983).
- [57] A. Kundu, N. Mingo, D. A. Broido, and D. A. Stewart, *Role of light and heavy embedded nanoparticles on the thermal conductivity of SiGe alloys*, *Phys. Rev. B* **84**, 125426 (2011).
- [58] M. Berglund and M. E. Wieser, *Isotopic compositions of the elements 2009 (IUPAC technical report)*, *Pure Appl. Chem.* **83**, 397–410 (2011).
- [59] Z. Wang and N. Mingo, *Absence of Casimir regime in two-dimensional nanoribbon phonon conduction*, *Appl. Phys. Lett.* **99**, 101903 (2011).
- [60] X. Yang, J. Carrete, and Z. Wang, *Role of force-constant difference in phonon scattering by nano-precipitates in PbTe*, *J. Appl. Phys.* **118**, 085701 (2015).

- [61] A. A. Maradudin, E. W. Montroll, G. H. Weiss, and I. P. Ipatova, *Theory of Lattice Dynamics in the Harmonic Approximation* (Academic Press, New York, 1971).
- [62] O. Madelung, *Introduction to solid-state theory* (Springer-Verlag, 1996), 3 edn.
- [63] G. Kresse, J. Furthmüller, and J. Hafner, *Ab-initio force constant approach to phonon dispersion relations of diamond and graphite*, Europhys. Lett. **32**, 729 (1995).
- [64] M. Gajdoš, K. Hummer, G. Kresse, J. Furthmüller, and F. Bechstedt, *Linear optical properties in the projector-augmented wave methodology*, Phys. Rev. B **73**, 045112 (2006).
- [65] H. T. Stokes, *Using symmetry in frozen phonon calculations*, Ferroelectrics **164**, 183–188 (1995).
- [66] L. L. Boyer, H. T. Stokes, and M. J. Mehl, *Self-Consistent potential induced breathing model calculations for longitudinal modes in MgO*, Ferroelectrics **164**, 177–181 (1995).
- [67] T. Feng and X. Ruan, *Quantum mechanical prediction of four-phonon scattering rates and reduced thermal conductivity of solids*, Phys. Rev. B **93**, 045202 (2016).
- [68] L. Lindsay, *First Principles Peierls-Boltzmann Phonon Thermal Transport: A Topical Review*, Nanosc. Microsc. Therm. **20**, 67–84 (2016).
- [69] K. Esfarjani and H. T. Stokes, *Method to extract anharmonic force constants from first principles calculations*, Phys. Rev. B **77**, 144112 (2008).
- [70] D. Lovelock and H. Rund, *Tensors, Differential Forms, and Variational Principles* (Dover Publications, 1975).
- [71] G. Kresse and J. Hafner, *Ab initio molecular dynamics for liquid metals*, Phys. Rev. B **47**, 558–561 (1993).
- [72] P. E. Blöchl, *Projector augmented-wave method*, Phys. Rev. B **50**, 17953–17979 (1994).
- [73] J. P. Perdew, K. Burke, and M. Ernzerhof, *Generalized Gradient Approximation Made Simple*, Phys. Rev. Lett. **77**, 3865–3868 (1996).
- [74] P. Nath, J. J. Plata, D. Usanmaz, R. Al Rahal Al Orabi, M. Fornari, M. Buongiorno Nardelli, C. Toher, and S. Curtarolo, *High-Throughput Prediction of Finite-Temperature Properties using the Quasi-Harmonic Approximation*, Comput. Mater. Sci. **125**, 82–91 (2016).
- [75] T. R. Anthony, W. F. Banholzer, J. F. Fleischer, L. Wei, P. K. Kuo, R. L. Thomas, and R. W. Pryor, *Thermal diffusivity of isotopically enriched  $^{12}\text{C}$  diamond*, Phys. Rev. B **42**, 1104–1111 (1990).
- [76] L. Wei, P. K. Kuo, R. L. Thomas, T. R. Anthony, and W. F. Banholzer, *Thermal conductivity of isotopically modified single crystal diamond*, Phys. Rev. Lett. **70**, 3764–3767 (1993).
- [77] Y. S. Touloukian, R. W. Powell, C. Y. Ho, and P. G. Klemens, *Thermophysical Properties of Matter - the TPRC Data Series*. (IFI/Plenum, 1970-1979).
- [78] J. A. Carruthers, T. H. Geballe, H. M. Rosenberg, and J. M. Ziman, *The Thermal Conductivity of Germanium and Silicon between 2 and 300 K*, Proc. R. Soc. A Math. Phys. Eng. Sci. **238**, 502–514 (1957).
- [79] D. T. Morelli and G. A. Slack, *High Lattice Thermal Conductivity Solids*, in *High Thermal Conductivity Materials*, edited by S. L. Shindé and J. S. Goela (Springer, 2006).
- [80] P. A. Popov, P. P. Fedorov, and V. V. Osiko, *Thermal conductivity of single crystals with a fluorite structure: Cadmium fluoride*, Phys. Solid State **52**, 504–508 (2010).
- [81] J. P. Moore, F. J. Weaver, R. S. Graves, and D. L. McElroy, *The Thermal Conductivities of  $\text{SrCl}_2$  and  $\text{SrF}_2$  from 85 to 400 K*, in *Thermal Conductivity*, edited by T. Ashworth and D. R. Smith (Springer US, 1985), pp. 115–124.
- [82] J. J. Martin and H. R. Shanks, *Thermal conductivity of magnesium plumbide*, J. Appl. Phys. **45**, 2428–2431 (1974).
- [83] A. R. Jha, *Rare Earth Materials: Properties and Applications* (CRC Press, 2014).
- [84] M. Mann, D. Thompson, K. Serivalsatit, T. M. Tritt, J. Ballato, and J. Kolis, *Hydrothermal Growth and Thermal Property Characterization of  $\text{ThO}_2$  Single Crystals*, Cryst. Growth Des. **10**, 2146–2151 (2010).
- [85] Z. Wang, J. E. Alaniz, W. Jang, J. E. Garay, and C. Dames, *Thermal Conductivity of Nanocrystalline Silicon: Importance of Grain Size and Frequency-Dependent Mean Free Paths*, Nano Lett. **11**, 2206–2213 (2011).
- [86] G. A. Slack, *Thermal conductivity of  $\text{CaF}_2$ ,  $\text{MnF}_2$ ,  $\text{CoF}_2$ , and  $\text{ZnF}_2$  crystals*, Phys. Rev. **122**, 1451–1464 (1961).
- [87] K. Schmalzl, D. Strauch, and H. Schober, *Lattice-dynamical and ground-state properties of  $\text{CaF}_2$  studied by inelastic neutron scattering and density-functional methods*, Phys. Rev. B **68**, 144301 (2003).
- [88] M. M. Elcombe and A. W. Pryor, *The lattice dynamics of calcium fluoride*, J. Phys. C: Solid State Phys. **3**, 492 (1970).
- [89] W. Kaiser, W. G. Spitzer, R. H. Kaiser, and L. E. Howarth, *Infrared Properties of  $\text{CaF}_2$ ,  $\text{SrF}_2$ , and  $\text{BaF}_2$* , Phys. Rev. **127**, 1950–1954 (1962).
- [90] J. Heyd, G. E. Scuseria, and M. Ernzerhof, *Hybrid functionals based on a screened Coulomb potential*, J. Chem. Phys. **118**, 8207–8215 (2003).
- [91] M. Shishkin, M. Marsman, and G. Kresse, *Accurate Quasiparticle Spectra from Self-Consistent GW Calculations with Vertex Corrections*, Phys. Rev. Lett. **99**, 246403 (2007).
- [92] M. Lazzeri, C. Attaccalite, L. Wirtz, and F. Mauri, *GW corrections to phonon dispersions*, Phys. Rev. B **78**, 081406 (2008).
- [93] K. Hummer, J. Harl, and G. Kresse, *Heyd-Scuseria-Ernzerhof hybrid functional for calculating the lattice dynamics of semiconductors*, Phys. Rev. B **80**, 115205 (2009).
- [94] C. Cazorla and D. Errandonea, *Superionicity and Polymorphism in Calcium Fluoride at High Pressure*, Phys. Rev. Lett. **113**, 235902 (2014).
- [95] L. Sang, M. Liao, Y. Koide, and M. Sumiya, *High-performance metal-semiconductor-metal  $\text{InGaN}$  photodetectors using  $\text{CaF}_2$  as the insulator*, Appl. Phys. Lett. **98**, 103502 (2011).
- [96] A. Lyberis, A. J. Stevenson, A. Sukanuma, S. Ricaud, F. Druon, F. Herbst, D. Vivien, P. Gredin, and M. Mortier, *Effect of  $\text{Yb}^{3+}$  concentration on optical properties of  $\text{Yb}:\text{CaF}_2$  transparent ceramics*, Opt. Mat. **34**, 965–968 (2012).
- [97] A. Supka, T. Lyons, L. Liyange, P. D’Amico, R. Al Rahal Al Orabi, S. Mahatara, P. Gopal, D. Ceseroli, A. Calzolari, C. Toher, S. Curtarolo, M. Buongiorno Nardelli, and M. Fornari, *AFLow $\pi$ : A minimalist approach to high-throughput ab initio calculations including the generation of tight-binding hamiltonians*, in preparation.
- [98] D. S. Sholl and J. A. Steckel, *Density Functional Theory: A Practical Introduction* (Wiley, 2009).